Influence of interface conditions on hydrogen transport studies

Rémi Delaporte-Mathurin, Etienne A Hodille, Jonathan Mougenot, Y. Charles, Gregory de Temmerman, Floriane Leblond, Christian Grisolia

HAL Id: hal-03188511

https://hal.science/hal-03188511

Submitted on 2 Apr 2021

Influence of interface conditions on hydrogen transport studies

Rémi Delaporte-Mathurin[a,b,*], Etienne A. Hodille[a], Jonathan Mougenot[b], Yann Charles[b], Gregory De Temmerman[c], Floriane Leblond[a], Christian Grisolia[a]

[a]*CEA, IRFM/GCFPM, F-13108 Saint-Paul-lez-Durance, France*
[b]*Université Sorbonne Paris Nord, Laboratoire des Sciences des Procédés et des Matériaux, LSPM, CNRS, UPR 3407, F-93430, Villetaneuse, France*
[c]*ITER Organization, Route de Vinon sur Verdon, CS 90 046, 13067, St Paul Lez Durance Cedex, France*

Abstract

This work investigates the influence of hydrogen chemical potential continuity across solid material interfaces. The implementation of the mathematical model in FESTIM is verified using the Method of Exact Solutions (MES) and the Method of Manufactured Solutions (MMS) in 1D, 2D, with complex material properties and inhomogeneous temperature fields. A comparison test between FESTIM, TMAP7 and Abaqus codes is also performed and the codes show good agreement. The chemical potential continuity condition has an impact up to 40% on the outgassing particle flux on 4 mm composite slabs (W/Cu and Cu/EUROFER) compared to mobile concentration continuity. A method for rapid identification of materials properties from outgassing flux measurements is given. The influence of chemical potential conservation on monoblock inventory is then studied. It is shown that, for the 1D and 2D ITER divertor monoblocks cases, discrepancies only start to appear after approximately 5×10^6 s of full power.

Keywords: Hydrogen transport, multi-material, Plasma Facing Component, 2D modelling, EUROFER, FESTIM

1. Introduction

In fusion devices, tritium transport in materials is a crucial issue for it can lead to system contamination, fuel losses [1], performance losses [2] and materials embrittlement [3]. For safety issues, the in-vessel safety limit for tritium inventory is 1 kg [4]. To this end, numerical modelling is often required in order to simulate complex geometries of plasma-facing components [5, 6, 7] and understand the fuel migration in various components. These components are often made of several materials joined together. This is the case for the monoblock geometry used for the ITER divertor which is made of a W armour, a CuCrZr cooling pipe jointed by a Cu inter-layer but also for DEMO breeding blankets since current designs involve W and EUROFER but Lithium, Beryllium, and other materials can also be found in some designs [8]. This study focuses on the interfaces between these materials, the physics at stake and their approximations.

Many hydrogen diffusion studies are focused on the gas-solid interfaces [9, 10, 11] using Sievert's law to ensure the hydrogen chemical potential continuity across interfaces. However, only few are focused on solid-solid interfaces [12, 7, 13, 14]. Several previous studies handled these interfaces by ensuring the continuity of the solute hydrogen particles concentration for simplification purposes

[7, 14]. Liu et al. [15] extended the Sievert's law to solid-solid interface, based on the mass-diffusion procedure of the Abaqus code [16]. The ratio between the solute concentration and the solubility is used to convey the conservation of chemical potential across interfaces. This kind of interface condition has also been implemented in hydrogen diffusion codes used for fusion applications TMAP7 [17]. Elmukashfi et al. [13] proposed a more complex model directly ensuring the continuity of the chemical potential. In this model, the reference hydrogen chemical potential must be known. These reference states depend on the material and are functions of the solubility [18].

The model of chemical potential conservation across interfaces and the approach adopted in this study to implement this model are described in Section 2. The implementation of this model in the hydrogen transport code FESTIM [7] is thoroughly verified in Section 3. The effect of chemical potential conservation on the outgassing flux of a composite slab is then studied in Section 4 with the code FESTIM. Finally, an application on the ITER monoblock test case is performed in order to assess the impact of interface conditions on the hydrogen inventory (see Section 5). A comparison test is also performed between FESTIM, TMAP7 [17] and the finite element suite Abaqus [5].

2. Interface model

According to [10] since the solubility of hydrogen atoms in solids is low, the chemical potential of solute hydrogen

---

μ is expressed by:

$$\mu = \mu_0 + RT \ln\left(\frac{c_{\mathrm{m}}}{N_L}\right) \tag{1}$$

where μ_0 is the chemical potential in a reference state in $\mathrm{J\,mol^{-1}}$, R the ideal gas constant, T the temperature in K, c_{m} the mobile hydrogen concentration in $\mathrm{m^{-3}}$ and N_L the lattice site concentration in $\mathrm{m^{-3}}$.

Assuming that only free hydrogen atoms contribute to the overall flux in the material, the particle flux J in $\mathrm{m^{-2}\,s^{-1}}$ can be expressed by Fick's law:

$$J = -D\nabla c_{\mathrm{m}} \tag{2}$$

where D is the diffusion coefficient of hydrogen in a non-stress lattice expressed in $\mathrm{m^2\,s^{-1}}$.

The local equilibrium at the interface between two materials must ensure the continuity of both the chemical potential μ (see Equation 3) and the particle flux (see Equation 4).

$$\mu^- = \mu^+ \tag{3}$$

$$D^-\nabla c_{\mathrm{m}}^- = D^+\nabla c_{\mathrm{m}}^+ \tag{4}$$

The chemical potential continuity can also be ensured by the continuity of the quantity c_{m}/S (see Equation 5) for mechanical stress-free materials in thermodynamic equilibrium and the Soret effect being neglected:

$$\left(\frac{c_{\mathrm{m}}}{S}\right)^- = \left(\frac{c_{\mathrm{m}}}{S}\right)^+ \tag{5}$$

Here, the quantity c_{m}/S, with S the solubility of hydrogen expressed in $\mathrm{m^{-3}\,Pa^{-0.5}}$, is equivalent to the root square of the pressure of an imaginary gas in thermodynamic equilibrium between the two solids and for which Sievert's law is applied. This assumption is correct as long as the time needed to reach the equilibrium is low compared to the time of the simulation. Appendix A described the characteristic time calculated by a transient interface model. For long exposure time (as in Section 5) as well as for high temperatures, it is shown that the characteristic time is small enough for the equilibrium model to be valid.

From Equation 5, one can deduce that a solubility discontinuity across an interface induces a discontinuity of mobile hydrogen concentration c_{m}. This can also be interpreted as the chemical potentials at a reference state being different in different materials [18], as the lattice site concentration.

To ensure a correct treatment of the material interface in hydrogen transport codes, two approaches can be employed. The most straightforward approach is to solve the hydrogen mobile concentration transport in both materials (see Equation 6) and enforce the concentration jump at the interface between the two materials with an internal condition verifying Equation 5 [17].

$$\frac{\partial c_{\mathrm{m}}}{\partial t} = \nabla \cdot (D\nabla c_{\mathrm{m}}) + f \tag{6}$$

where f is the source term in $\mathrm{m^{-3}\,s^{-1}}$.

Another method is to perform a change of variable in Fick's second law of diffusion with $\phi = c_{\mathrm{m}}/S$ [16] when internal conditions cannot be set. Equation 6 therefore reads:

$$\begin{aligned}\frac{\partial \phi S}{\partial t} &= \nabla \cdot (D\nabla \phi S) + f \\ &= \nabla \cdot (DS\nabla\phi + D\phi\nabla S) + f\end{aligned} \tag{7}$$

Because ϕ is computed, the ratio c_{m}/S is continuous by default at the material interfaces.

This second approach is used for instance in the *mass-diffusion* procedure of the Abaqus code. However, this procedure cannot be directly used to simulate hydrogen transport with thermomechanical loading *(coupled temperature displacement* procedure) [16]. Indeed, the *mass-diffusion* procedure can solve mechanically-assisted diffusion problems, knowing the spatio-temporal evolution of the mechanical pressure. The *temperature-displacement* procedure is used to simultaneously solve diffusion and mechanical problems. To account for both mechanical fields, trapping influence on diffusion and transient heat transfer, User Subroutines are employed. Appendix B describes the implementation based on user Subroutines. This interface model has also been implemented into the current hydrogen transport code FESTIM [7] using FEniCS [19].

All plots in this work were generated with Matplotlib [20].

3. Analytical verification

To ensure the implementation of the interface model in FESTIM is error free, analytical verification is required since physical trend tests are not rigorous enough. The verification process aims at checking the code is correctly solving the governing Equations 4, 5, 6 and 7. To this end, two methods were used: the Method of Exact Solutions (MES) and the Method of Manufactured Solutions (MMS). It is worth noting that these two methods do not require to be physically realistic since this is a purely mathematical exercise. In practice, not having real life properties or realistic domain sizes can even facilitate the construction of a general test case and therefore ease the results reproduction by others. A complete H transport problem would include coupling with trapping/detrapping (as in Section 5). The implementation of the trapping/detrapping coupling in FESTIM has already been analytically verified in [7] therefore this Section will only focus on verifying the solving of Equations 4, 5, 6 and 7.

3.1. Method of Exact Solutions (MES)

The uni-dimensional test case considered in this Section was made of two subdomains Ω_1 and Ω_2 and is de-

scribed as follow:

$$\Omega = [0, L] = \Omega_1 \cup \Omega_2 \tag{8a}$$

$$\Omega_1 = [0, x_{\text{int}}] \tag{8b}$$

$$\Omega_2 = [x_{\text{int}}, L] \tag{8c}$$

$$D = \begin{cases} D_1, & \text{in } \Omega_1 \\ D_2, & \text{in } \Omega_2 \end{cases} \tag{8d}$$

$$S = \begin{cases} S_1, & \text{in } \Omega_1 \\ S_2, & \text{in } \Omega_2 \end{cases} \tag{8e}$$

The following dimensionless quantities are introduced:

$$\tilde{c}_{\text{m}} = c_{\text{m}}/c_0 \tag{9a}$$

$$\tilde{x} = x/L \tag{9b}$$

$$\tilde{f} = f \frac{L^2}{D_{\text{eq}} c_0} \tag{9c}$$

$$\alpha = D_2/D_1 \tag{9d}$$

$$\beta = S_2/S_1 \tag{9e}$$

$$\gamma = x_{\text{int}}/L \tag{9f}$$

$$\tag{9g}$$

where $D_{\text{eq}} = (D_1 D_2)^{1/2}$.

By integrating Equation 6 and assuming steady-state (i.e. $\partial c/\partial t = 0$), one can obtain the following dimensionless form:

$$\tilde{c}_{\text{m}} = \begin{cases} -\frac{1}{2}\alpha^{1/2}\tilde{f}\tilde{x}^2 + a_1\tilde{x} + b_1, & \text{in } \Omega_1 \\ -\frac{1}{2}\alpha^{-1/2}\tilde{f}\tilde{x}^2 + a_2\tilde{x} + b_2, & \text{in } \Omega_2 \end{cases} \tag{10}$$

where a_1, b_1, a_2, b_2 are the unknowns of the problem to be determined. The boundary conditions and the equilibrium law at the interface are defined as:

$$\tilde{c}_{\text{m}}(\tilde{x} = 0) = 1 \tag{11a}$$

$$\tilde{c}_{\text{m}}(\tilde{x} = 1) = \tilde{c}_L \tag{11b}$$

$$\tilde{c}_{\text{m}}^-(\tilde{x} = \gamma) = \beta\, \tilde{c}_{\text{m}}^+(\tilde{x} = \gamma) \tag{11c}$$

$$\nabla \tilde{c}_{\text{m}}^-(\tilde{x} = \gamma) = \alpha \nabla \tilde{c}_{\text{m}}^+(\tilde{x} = \gamma) \tag{11d}$$

Equation 10 can be solved with these constraints and coefficients describing c_{m} therefore read:

$$\begin{aligned} a_1 &= a_0\, \alpha^{1/2} \\ b_1 &= 1 \\ a_2 &= a_0\, \alpha^{-1/2} \\ b_2 &= \tilde{c}_L + \frac{1}{2}\alpha^{-1/2}\tilde{f} - a_2 \\ a_0 &= \frac{2\alpha^{1/2}(\tilde{c}_L - \beta) + \tilde{f}(\gamma^2(1 - \alpha\beta) - 1)}{2(1 + \alpha\beta - \gamma)} \end{aligned} \tag{12}$$

It is worth noting that when $\beta = 1$ (i.e. $S_1 = S_2 = S$) the solution becomes independent of S and $c_{\text{m}}^-(x_{\text{int}}) =$

$c_{\text{m}}^+(x_{\text{int}})$. Moreover, when $\alpha = 1$ (i.e. $D_1 = D_2 = D$), then $a_1 = a_2 = a_0$ which is the solution for steady-state diffusion in a mono-material.

The solution computed by FESTIM was found to be in very good agreement with the analytical solution for several test cases (see Figure 1).

However, this method does not exercise all the terms in the governing Equation 7. For instance, this analytical solution is only uni-dimensional, steady state is assumed and material properties are constant within the materials. Having an exact solution from an analytical resolution for a general problem (multidimensional, transient, heterogeneous material properties, etc...) is often complex. In order to exercise all these terms, the Method of Manufactured Solutions (MMS) will therefore be employed for it offers a good alternative to unravel these complexities.

3.2. Method of Manufactured Solutions (MMS)

The goal of Method of Manufactured Solutions (MMS) is to have an exact solution which is general enough to exercise all the terms of the governing equations. This method also allows to test the implementation of the FESTIM code on a multidimensional problem.

The domain Ω for this test problem is a unit square composed of two subdomains Ω_1 and Ω_2 (see Equation 13).

$$\Omega = [0, 1] \times [0, 1] \tag{13a}$$

$$\Omega_1 = [0, x_{\text{int}}] \times [0, 1] \tag{13b}$$

$$\Omega_2 = [x_{\text{int}}, 1] \times [0, 1] \tag{13c}$$

$$\tag{13d}$$

In order to unravel the complexity of an analytical resolution of the direct problem, a manufactured solution c_M was constructed (see Equation 14) and the problem was solved backwards.

$$c_M = \begin{cases} c_{M1}, & \text{on } \Omega_1 \\ \frac{S_2}{S_1} \cdot c_{M1}, & \text{on } \Omega_2 \end{cases} \tag{14}$$

where $c_{M1} = 2 + \cos(2\pi x) \cdot \cos(2\pi y) + t$

It is worth noting that, when choosing a manufactured solution, one must ensure it satisfies all the governing equations (especially Equations 4 and 5). In our case, c_M ensures the flux conservation at the interface and the continuity of the quantity c_{m}/S.

Properties are assumed time and space dependent in order to test every portion of the code (see Equation 15).

$$D_1(x, y, t) = D_{1_0} \exp(-E_{D_1}/(k_B \cdot T(x, y, t))) \tag{15a}$$

$$D_2(x, y, t) = D_{2_0} \exp(-E_{D_2}/(k_B \cdot T(x, y, t))) \tag{15b}$$

$$S_1(x, y, t) = S_{1_0} \exp(-E_{S_1}/(k_B \cdot T(x, y, t))) \tag{15c}$$

$$S_2(x, y, t) = S_{2_0} \exp(-E_{S_2}/(k_B \cdot T(x, y, t))) \tag{15d}$$

$$T(x, y, t) = 500 + 30\cos(2\pi x)\cos(2\pi y)\cos(2\pi t) \tag{15e}$$

with $k_B = 8.617 \times 10^{-5}\,\text{eV K}^{-1}$ the Boltzmann constant, $D_{1_0} = 1$, $E_{D_1} = 0.1$, $D_{2_0} = 2$, $E_{D_2} = 0.2$, $S_{1_0} = 1$,

$E_{S_1} = 0.1$, $S_{2_0} = 2$ and $E_{S_2} = 0.2$. The temperature T varies around $500\,\mathrm{K}$ so that, given the activation energies, properties do not approach zero.

By injecting the manufactured solution c_M into the governing Equation 6, the source term can be expressed as:

$$f(x, y, t) = \frac{\partial c_M}{\partial t} - \vec{\nabla} \cdot \left(D(x, y) \vec{\nabla} c_M \right)$$

$$= \begin{cases} \frac{\partial c_{M_1}}{\partial t} - \vec{\nabla} \cdot \left(D_1(x, y) \vec{\nabla} c_{M_1} \right), & \text{on } \Omega_1 \\ \frac{\partial c_{M_2}}{\partial t} - \vec{\nabla} \cdot \left(D_2(x, y) \vec{\nabla} c_{M_2} \right), & \text{on } \Omega_2 \end{cases}$$

$$(16)$$

The source term f was then fed into FESTIM alongside with the initial and boundary conditions described below:

$$c_{\mathrm{m}}(x, y, t) = c_M(x, y, t), \text{ on } \partial\Omega \tag{17a}$$

$$c_{\mathrm{m}}(x, y, t = 0) = c_M(x, y, t = 0), \text{ on } \Omega \tag{17b}$$

The computed solution c_{comp} can then be compared with the manufactured solution c_M in order to quantitatively measure the numerical error. After running the MMS process, the computed solution and the manufactured solution were in very good agreement at several arbitrarily chosen times of simulation (see Figure 2). The absolute difference between the manufactured solution and the computed one was found to be zero on the boundary and maximum at the interface between the two materials. This is explained by the Dirichlet boundary conditions enforcing the computed solution on the boundary. This difference decreases by increasing the mesh refinement and decreasing the stepsize. Nonetheless, the error was found to remain orders of magnitude lower than the actual solution.
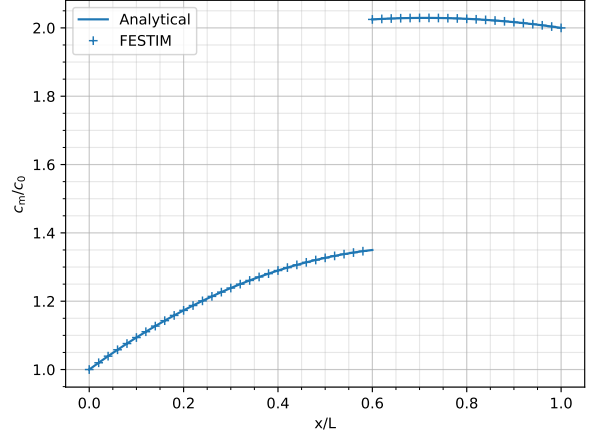
(a) Case 1: $\alpha = 2$, $\beta = 1.5$, $\gamma = 0.6$, $\tilde{c}_L = 2$, $\tilde{f} = 1$
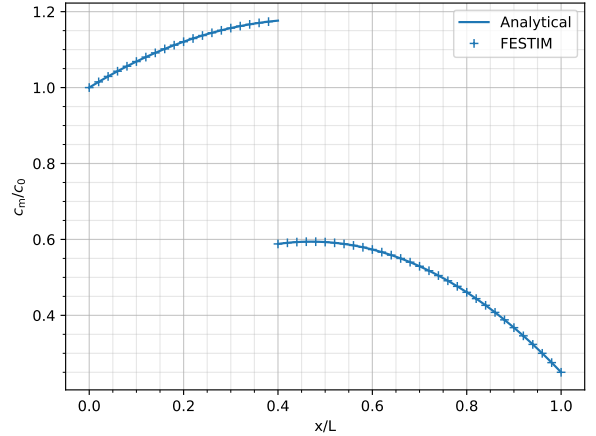
(b) Case 2: $\alpha = 1.5$, $\beta = 0.5$, $\gamma = 0.4$, $\tilde{c}_L = 0.25$, $\tilde{f} = 2$

Figure 1: Concentration profiles simulated by FESTIM against analytical solutions.

(a) Computed solution $c_{\text{comp}}(t = 0.01)$

(b) Exact solution $c_M(t = 0.01)$

(c) Absolute difference

(d) Computed solution $c_{\text{comp}}(t = 0.06)$

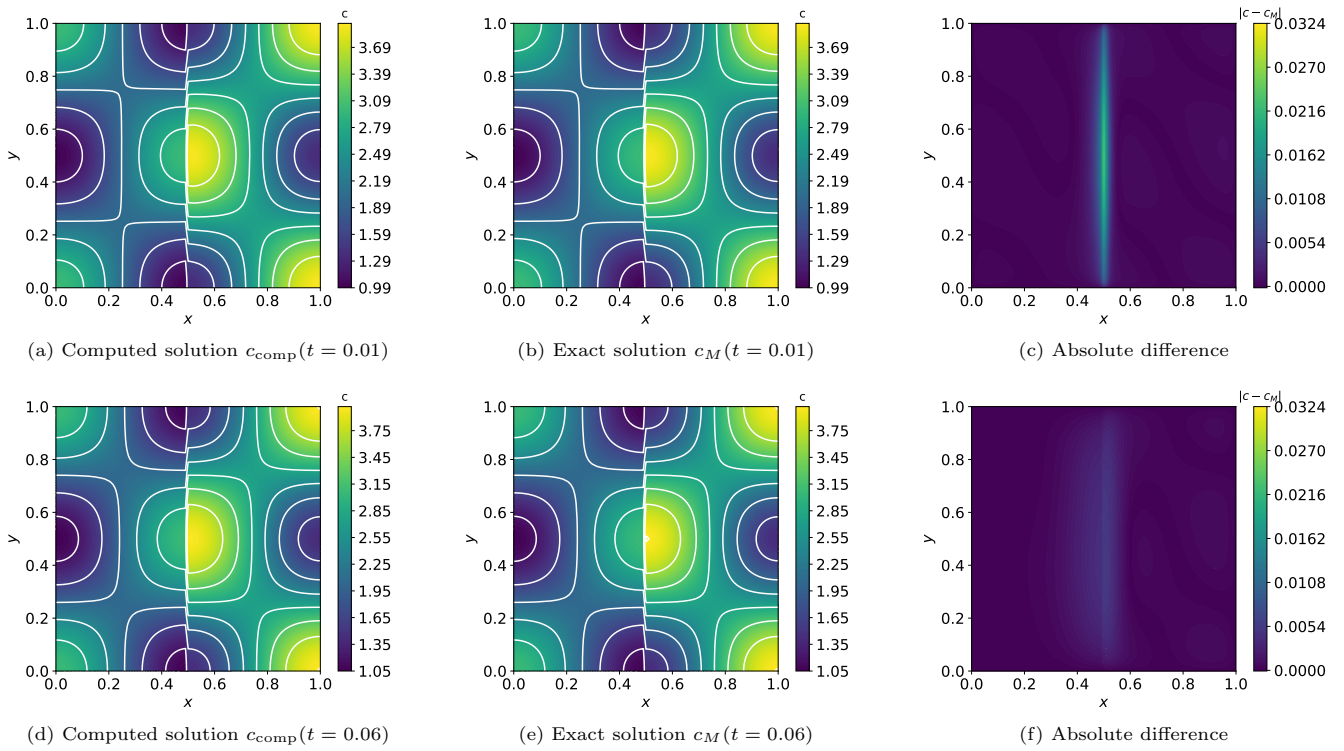(e) Exact solution $c_M(t = 0.06)$

(f) Absolute difference

Figure 2: Comparison of concentration fields simulated by FESTIM with manufactured solutions

4. Influence of chemical potential continuity on outgassing flux

In order to assess the influence of interface conditions on the outgassing flux, simulations are performed with chemical potential continuity (Equation 5) or mobile concentration continuity assuming in both cases flux conservation (Equation 4). For the sake of simplicity and to emphasis on the influence of interface conditions, no trapping was assumed and idea Dirichlet boundary conditions were set. Simulations were performed on two test cases: W/Cu and Cu/EUROFER. The materials properties used for the simulations can be found in Table 1. In both cases the solute concentration c_m was set to $1 \times 10^{20}\,\mathrm{m}^{-3}$ at $x = 0$ and zero on the other boundary.

4.1. W/Cu case

A $4\,\mathrm{mm}$-thick slab made of $2\,\mathrm{mm}$ of W (referred as Ω_1) and $2\,\mathrm{mm}$ of Cu (referred as Ω_2) at $T = 500\,\mathrm{K}$ was first simulated.

In this case, the conservation of chemical potential resulted in higher steady-state concentration gradients (see Figure 3a) due to the higher solubility of Cu. For a given temperature (and therefore given diffusion coefficients), this implied an increase of the outgassing flux (see Figure 3b) compared to the case with concentration continuity.

4.2. Cu/EUROFER case

A $4\,\mathrm{mm}$-thick slab made of $2\,\mathrm{mm}$ of Cu (referred as Ω_1) and $2\,\mathrm{mm}$ of EUROFER (referred as Ω_2) at $T = 600\,\mathrm{K}$ was simulated. Contrarily to the previous case, since the solubility of EUROFER is lower than that of Cu, the steady-state concentration gradients (see Figure 3c) were lower compared to the case with concentration continuity. The outgassing flux was therefore lower in the case of chemical potential conservation (see Figure 3d).

4.3. Identification technique

Assuming the diffusion coefficients are known, the solubility coefficients in both materials can be identified by determining an effective diffusion coefficient.

The steady-state flux φ_∞ can be expressed from Equations 10 and 12 as follow:

$$\varphi_\infty = -D_2 \nabla c_2 = -D_1 \nabla c_1 \tag{18a}$$

$$= -D_2 a_2 \frac{c_m(x=0)}{L} = -D_1 a_1 \frac{c_m(x=0)}{L} \tag{18b}$$

$$= -a_0 D_{eq} \frac{c_m(x=0)}{L} \tag{18c}$$

If this method allows to measure solubilities, it is however not always convenient considering the time required to reach steady-state. One way to overcome this difficulty is to compute an equivalent effective diffusion coefficient noted D_{eff}. D_{eff} is computed by assuming an homogeneous material and a linear steady state profile. The steady-state flux can therefore be written as:

$$\varphi_\infty = -D_{eff} \nabla c \tag{19a}$$

$$= -D_{eff} \frac{c_m(x=L) - c_m(x=0)}{L} \tag{19b}$$

$$\tag{19c}$$

By combining Equations 18 and 19, D_{eff} reads:

$$D_{eff} = \frac{a_0\, D_{eq}\, c_m(x=0)}{c_m(x=L) - c_m(x=0)} \tag{20}$$

By fitting measurements of the outgassing flux with either an analytical transient solution or a simulation code (see Figures 3b and 3d), one can estimate D_{eff} and therefore the coefficient a_0 which can finally be correlated to material properties (see Equation 12).

However, some discrepancies were found between this method and the actual outgassing curve during the transient phase. One way of getting rid of these is to fit the curve with an analytical solution of transient mass transfer in a 1D composite slab with conservation of chemical potential. This can be utterly complex and is well beyond the scope of this study.

Moreover, surface effects and the presence of traps often complicate the analysis of the experimental data. Therefore, a more thorough identification technique would be to use embedded hydrogen transport codes such as FESTIM in a parametric optimisation algorithm as described in previous work [21]. Such a process could be able to determine materials properties such as diffusion coefficients, solubilities and trap densities.
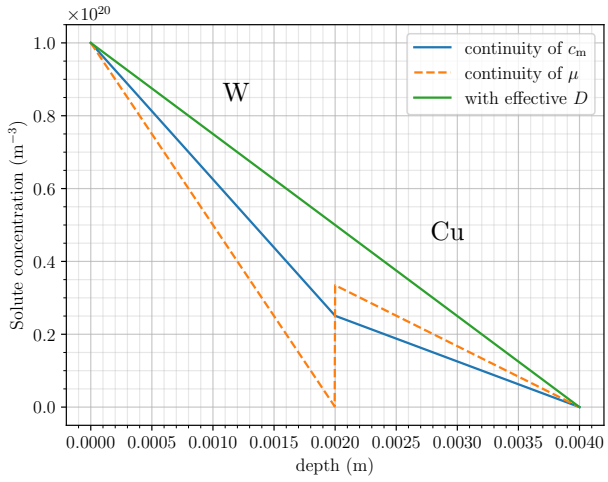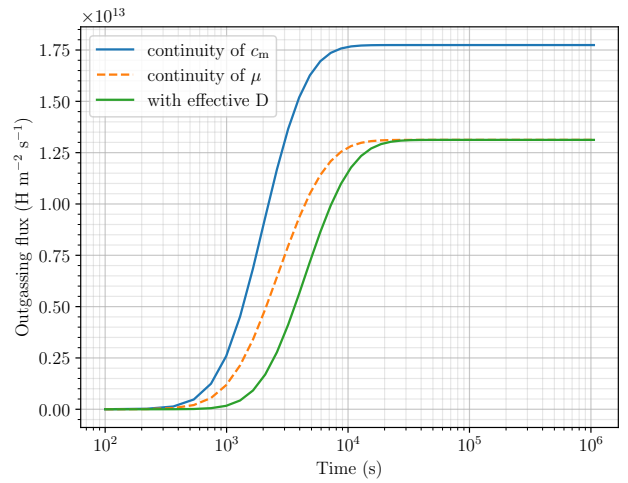
(a) Solute profiles at steady state (W/Cu)
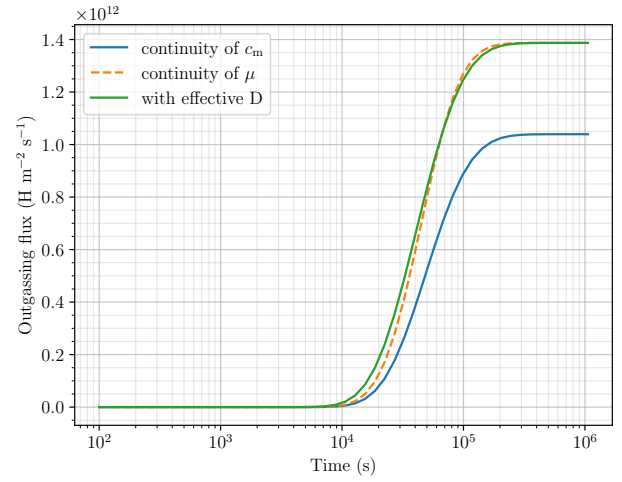
(b) Outgassing flux (W/Cu)
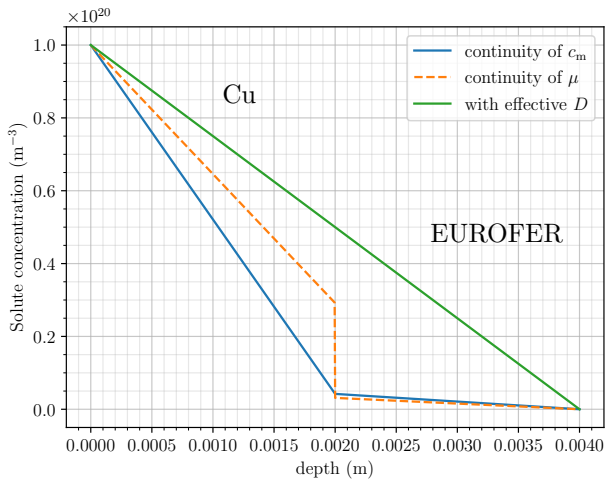
(c) Solute profiles at steady state (Cu/EUROFER)

(d) Outgassing flux (Cu/EUROFER)

Figure 3: Influence of chemical potential conservation

5. Application: ITER monoblock

This implementation of chemical potential continuity was applied to a test case in order to simulate hydrogen transport an ITER-like monoblock. For this application, trapping of hydrogen in defects was taken into account. The governing equations for hydrogen transport therefore read:

$$\frac{\partial c_{\mathrm{m}}}{\partial t} = \nabla \cdot (D(T)\nabla c_{\mathrm{m}}) + \varphi_{\mathrm{imp}} \cdot U(\mathbf{x}) - \sum \frac{\partial c_{\mathrm{t},i}}{\partial t} \quad (21a)$$

$$\frac{\partial c_{\mathrm{t},i}}{\partial t} = k(T) \cdot c_{\mathrm{m}} \cdot (n_i - c_{\mathrm{t},i}) - p(T) \cdot c_{\mathrm{t},i} \quad (21b)$$

where $D(T) = D_0 \cdot \exp\left(-E_{\mathrm{diff}}/(k_B \cdot T)\right)$ is the diffusion coefficient in $\mathrm{m^2\,s^{-1}}$, T the temperature in K and $k_B = 8.617 \times 10^{-5}\,\mathrm{eV\,K^{-1}}$ the Boltzmann constant, $c_{\mathrm{t},i}$ is the concentration in $\mathrm{m^{-3}}$ of particles trapped in the i-th trap,

$$k(T) = k_0 \exp\left(-E_k/(k_B \cdot T)\right) \quad (22)$$

and

$$p(T) = p_0 \exp\left(-E_p/(k_B \cdot T)\right) \quad (23)$$

are the trapping and detrapping rates expressed in $\mathrm{m^3\,s^{-1}}$ and $\mathrm{s^{-1}}$ respectively, n_i is the trap density in $\mathrm{m^{-3}}$, φ_{imp} is the implanted particle flux in $\mathrm{m^{-2}\,s^{-1}}$ and $U(\mathbf{x})$ is the spatial distribution of the implanted particle flux.

The thorough description of this model as well as the verification of its implementation in FESTIM is given in [7].

The source term φ_{imp} is equal to $5 \times 10^{23}\,\mathrm{m^{-2}\,s^{-1}}$ and its spatial distribution is:

$$U(\mathbf{x}) = \begin{cases} R_p^{-1}, & \text{if } x < R_p \\ 0, & \text{else} \end{cases} \quad (24)$$

where $R_p = 2.5\,\mathrm{nm}$ is the implantation range. Since the implantation range is very small compared to the monoblock dimensions, this source is equivalent to applying a Dirichlet boundary condition on the exposed surface [14]. The value of this boundary condition therefore depends on φ_{imp}, the implantation range R_p and the diffusion coefficient D.

The chemical potential is conserved across interfaces by ensuring Equations 4 and 5 where

$$S = S_0 \cdot \exp\left(-E_S/(k_B \cdot T)\right) \quad (25)$$

is the solubility coefficient in $\mathrm{m^{-3}\,Pa^{-0.5}}$.

A comparison test was first performed and the FESTIM code was compared to TMAP7 [17] and Abaqus on a 1D case. 2D simulations of ITER-like monoblocks were then performed. The influence of interface conditions on hydrogen inventory was studied in both cases.

The materials properties that have been set are detailed in Table 1 and their thermal dependency is shown on Figure 5. The trap properties in each material are detailed in Table 2. All traps are homogeneously distributed in the materials, except for Trap 2 which is only located in the first micrometre behind the plasma facing surface Γ_{top} (see Figure 4) to account for damage creation.

5.1. 1D case and comparison with TMAP7 and Abaqus

The 1D simulation case is a 8.5 mm-thick composite slab made of W, Cu and CuCrZr (see Figure 4a). The plasma facing surface Γ_{top} is located at $x = 0\,\mathrm{mm}$ and the surface cooled by water $\Gamma_{\mathrm{coolant}}$ is located at $x = 8.5\,\mathrm{mm}$.

The boundary conditions are detailed in Equation 26.

$$T = 1200\,\mathrm{K} \quad \text{on } \Gamma_{\mathrm{top}} \quad (26a)$$

$$c_{\mathrm{m}} = \frac{\varphi_{\mathrm{imp}} \cdot R_p}{D} \quad \text{on } \Gamma_{\mathrm{top}} \quad (26b)$$

$$T = 373\,\mathrm{K} \quad \text{on } \Gamma_{\mathrm{coolant}} \quad (26c)$$

$$-D\nabla c_{\mathrm{m}} \cdot \vec{n} = K_{\mathrm{CuCrZr}} \cdot c_{\mathrm{m}}^2 \quad \text{on } \Gamma_{\mathrm{coolant}} \quad (26d)$$

with $\varphi_{\mathrm{imp}} = 5 \times 10^{23}\,\mathrm{m^{-2}\,s^{-1}}$ the implanted particle flux, $R_p = 1.25\,\mathrm{nm}$ the implantation depth, $\vec{n}$ the normal vector and $K_{\mathrm{CuCrZr}} = 2.9 \times 10^{-14} \cdot \exp\left(-1.92/(k_B \cdot T)\right)$ the recombination coefficient of the CuCrZr (in vacuum) expressed in $\mathrm{m^4\,s^{-1}}$ [28].

The Dirichlet boundary condition on Γ_{top} for the hydrogen transport corresponds to a flux balance between the implanted flux and the flux that is retro-desorbed at the surface. The details can be found in [14].

A comparison test was made with the codes TMAP7 and Abaqus with this set of parameters and very good agreement was found between the two codes (see Figure 9).

Two simulations were run, one ensuring mobile concentration c_{m} continuity at interfaces and the other ensuring the continuity of chemical potential μ.

Up to $5 \times 10^6\,\mathrm{s}$, the total hydrogen inventory was found to be insensitive to the conservation of chemical potential (see Figure 7a). It is only after this implantation that the inventory of the simulation with continuity of chemical potential started to diverge. At $t = 2.4 \times 10^7\,\mathrm{s}$, the inventory with continuity of μ was more than two times higher than that of the one with continuity of c_{m}. This is explained by the high solubility ratio between Cu and CuCrZr leading to a higher concentration of mobile particles in CuCrZr and therefore a higher trapping rate. Before reaching the W/Cu interface, the c_{m} and retention profiles are identical regardless of the interface condition (see Figure 8). Once this interface is reached, the c_{m} profiles are affected by the interface condition. However, even then, the trap density in Cu being low compared to other materials, the global inventory is not affected much. For these two reasons, the inventories are identical before $5 \times 10^6\,\mathrm{s}$.

5.2. 2D case

The boundary conditions for the 2D case are similar with an additional Dirichlet boundary condition on $\Gamma_{\mathrm{lateral}}$. This boundary condition accounts for recombi-
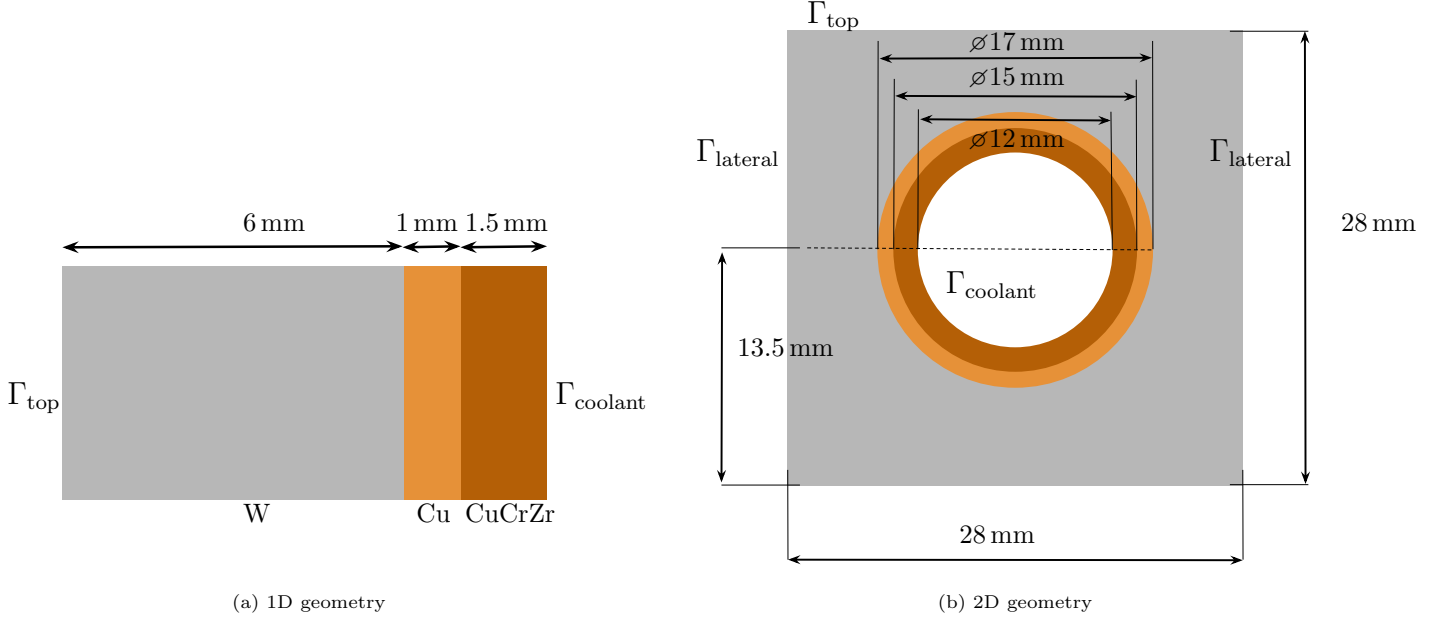
(a) 1D geometry
(b) 2D geometry

Figure 4: Monoblock geometry showing W armour ▮, Cu interlayer ▮, CuCrZr alloy cooling pipe ▮

nation on the lateral sides of the monoblock.

$$T = 1200\,\text{K} \quad \text{on } \Gamma_{\text{top}} \tag{27a}$$

$$c_{\text{m}} = \frac{\varphi_{\text{imp}} \cdot R_p}{D} \quad \text{on } \Gamma_{\text{top}} \tag{27b}$$

$$T = 373\,\text{K} \quad \text{on } \Gamma_{\text{coolant}} \tag{27c}$$

$$-D\nabla c_{\text{m}} \cdot \vec{n} = K_{\text{CuCrZr}} \cdot c_{\text{m}}^2 \quad \text{on } \Gamma_{\text{coolant}} \tag{27d}$$

$$c_{\text{m}} = 0 \quad \text{on } \Gamma_{\text{lateral}} \tag{27e}$$

with $\varphi_{\text{imp}} = 5 \times 10^{23}\,\text{m}^{-2}\,\text{s}^{-1}$ the implanted particle flux, $R_p = 1.25\,\text{nm}$ the implantation depth, $\vec{n}$ the normal vector and $K_{\text{CuCrZr}} = 2.9 \times 10^{-14} \cdot \exp\left(-1.92/(k_B \cdot T)\right)$ the recombination coefficient of the copper alloy (in vacuum) expressed in $\text{m}^4\,\text{s}^{-1}$ [28].

The concentrations fields (see Figure 10) showed results similar to those obtained in the 1D case (see Figure 8). The interface condition had no influence whatsoever on the mobile particle concentration c_{m} in the W. However, c_{m} was higher in Cu and CuCrZr in the case with chemical potential conservation (up to $1.5 \times 10^{24}\,\text{m}^{-3}$ in CuCrZr at $t = 2.4 \times 10^7\,\text{s}$). As in the 1D case, this increase of c_{m} lead to an increase of the trap occupancy and therefore an increase of the local retention.

The hydrogen inventories in the monoblock were found to be identical for most of the implantation time (see Figure 7b). It was only after $5 \times 10^6\,\text{s}$ that the inventory with chemical potential conservation was significantly higher than the one with c_{m} continuity at interfaces.

In both the 1D and 2D case, the flux which is retro-desorbed from the monoblock to the plasma does not depend on the interface conditions since interface are far from the exposed surface. Moreover, outgassing flux through the cooling pipe greatly depends on the boundary condition imposed at the cooling surface. Therefore, in order

to assess the impact of interface conditions on the outgassing flux through the cooling pipe, uncertainties must first be lift regarding the recombination process occurring on surfaces in contact with water.

9

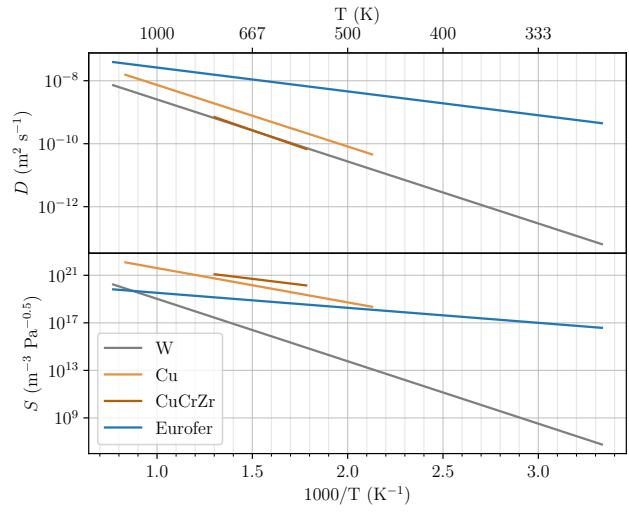|	Thermal properties		Hydrogen transport properties			
Material	$\rho \cdot C_p$ $(\mathrm{J\,K^{-1}\,m^{-3}})$	λ $(\mathrm{W\,K^{-1}})$	D_0 $(\mathrm{m^2\,s^{-1}})$	E_{diff} (eV)	S_0 $(\mathrm{m^{-3}\,Pa^{-0.5}})$	E_{S} (eV)
W [22]	$5.1 \times 10^{-6} \cdot T^3$ $- 8.3 \times 10^{-2} \cdot T^2$ $+ 6.0 \times 10^2 \cdot T$ $+ 2.4 \times 10^6$	$-7.8 \times 10^{-9} \cdot T^3$ $+ 5.0 \times 10^{-5} \cdot T^2$ $- 1.1 \times 10^{-1} \cdot T$ $+ 1.8 \times 10^2$	2.4×10^{-7}	0.39	1.87×10^{24}	1.04
Cu [23]	$1.7 \times 10^{-4} \cdot T^3$ $+ 6.1 \times 10^{-2} \cdot T^2$ $+ 4.7 \times 10^2 \cdot T$ $+ 3.5 \times 10^6$	$-3.9 \times 10^{-8} \cdot T^3$ $+ 3.8 \times 10^{-5} \cdot T^2$ $- 7.9 \times 10^{-2} \cdot T$ $+ 4.0 \times 10^2$	6.6×10^{-7}	0.39	3.14×10^{24}	0.57
CuCrZr [24]	$-1.8 \times 10^{-4} \cdot T^3$ $+ 1.5 \times 10^{-1} \cdot T^2$ $+ 6.2 \times 10^2 \cdot T$ $+ 3.5 \times 10^6$	$5.3 \times 10^{-7} \cdot T^3$ $- 6.5 \times 10^{-4} \cdot T^2$ $+ 2.6 \times 10^{-1} \cdot T$ $+ 3.1 \times 10^2$	3.9×10^{-7}	0.42	4.28×10^{23}	0.39
EUROFER [25]	-	-	1.5×10^{-7}	0.15	6.14×10^{20}	0.25

Table 1: Materials properties used in the simulations. Thermal properties are fitted from ANSYS.

	Material	$k_0(\mathrm{m^3\,s^{-1}})$	E_k(eV)	$p_0(\mathrm{s^{-1}})$	E_p(eV)	n_i(at fr)
Trap 1	W	3.8×10^{-17}	0.39	8.4×10^{12}	1.20	5.0×10^{-4}
Trap 2	W	3.8×10^{-17}	0.39	8.4×10^{12}	1.40	5.0×10^{-3}
Trap 3	Cu	6.0×10^{-17}	0.39	8.0×10^{13}	0.50	5.0×10^{-5}
Trap 4	CuCrZr	1.2×10^{-16}	0.42	8.0×10^{13}	0.50	5.0×10^{-5}
Trap 5	CuCrZr	1.2×10^{-16}	0.42	8.0×10^{13}	0.83	4.0×10^{-2}

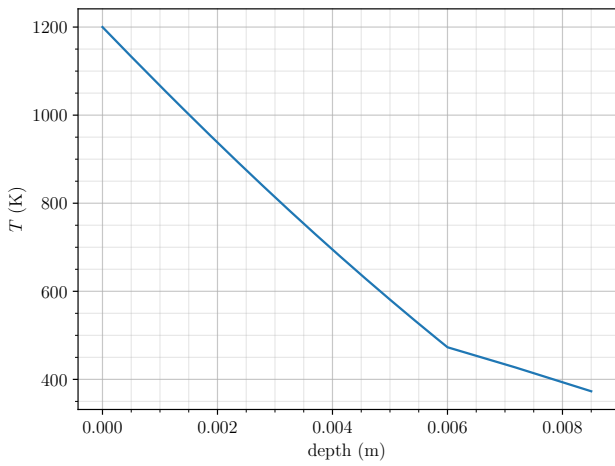Table 2: Traps properties used in the simulations [26, 27]
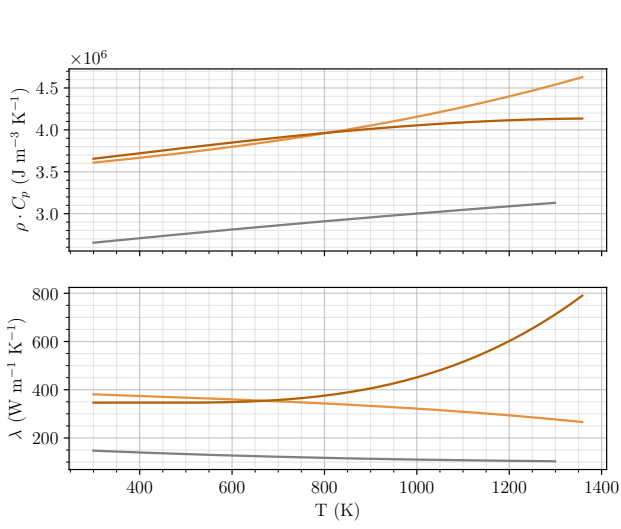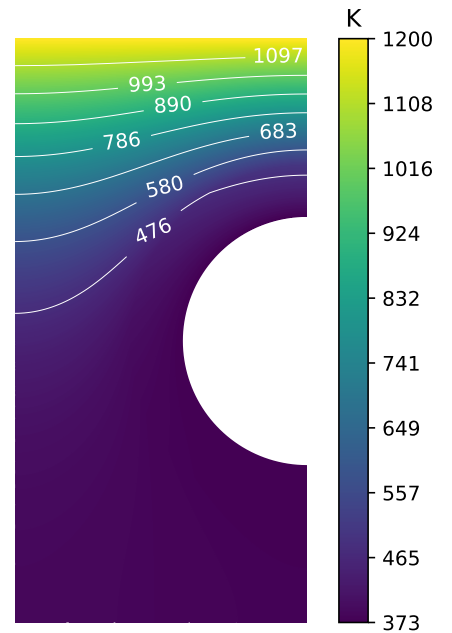
(a) Thermal properties

(b) H transport properties

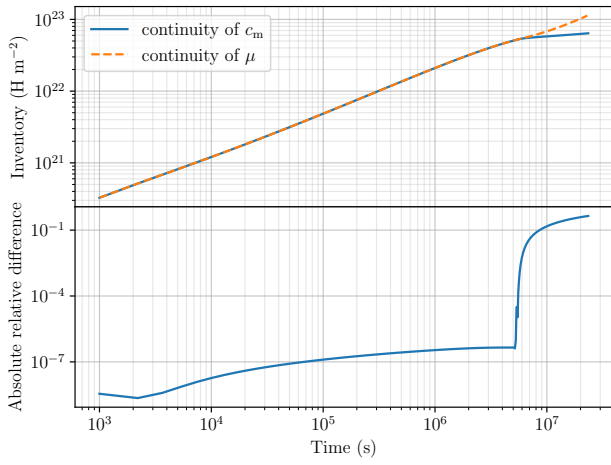Figure 5: Material properties used in the simulations [22, 23, 24, 25]
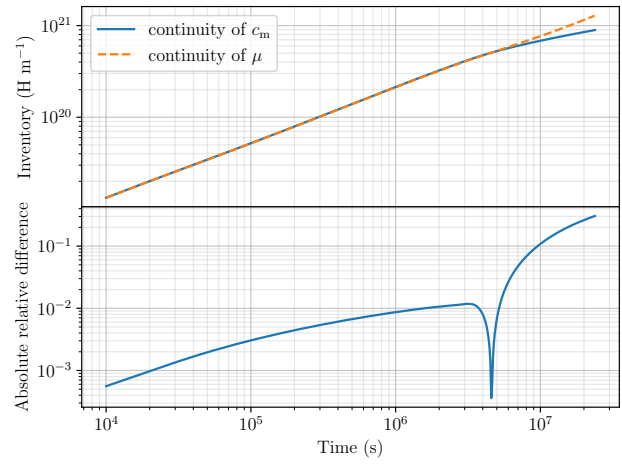

(a) 1D case

(b) 2D case

Figure 6: Monoblock temperature simulated by FESTIM

(a) 1D case

(b) 2D case

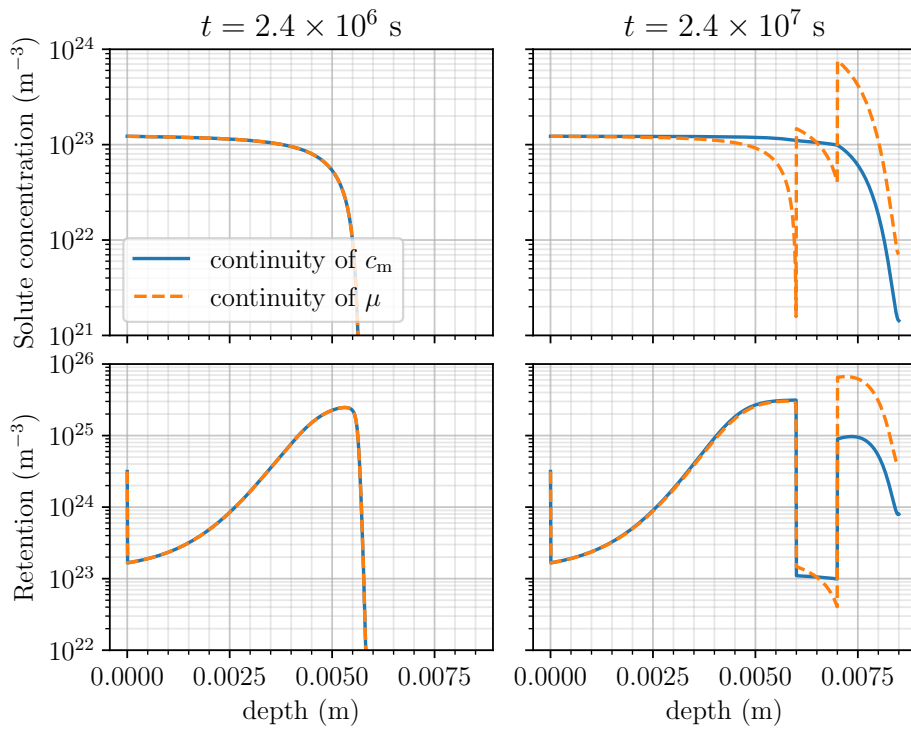Figure 7: Influence of chemical potential conservation on hydrogen inventory

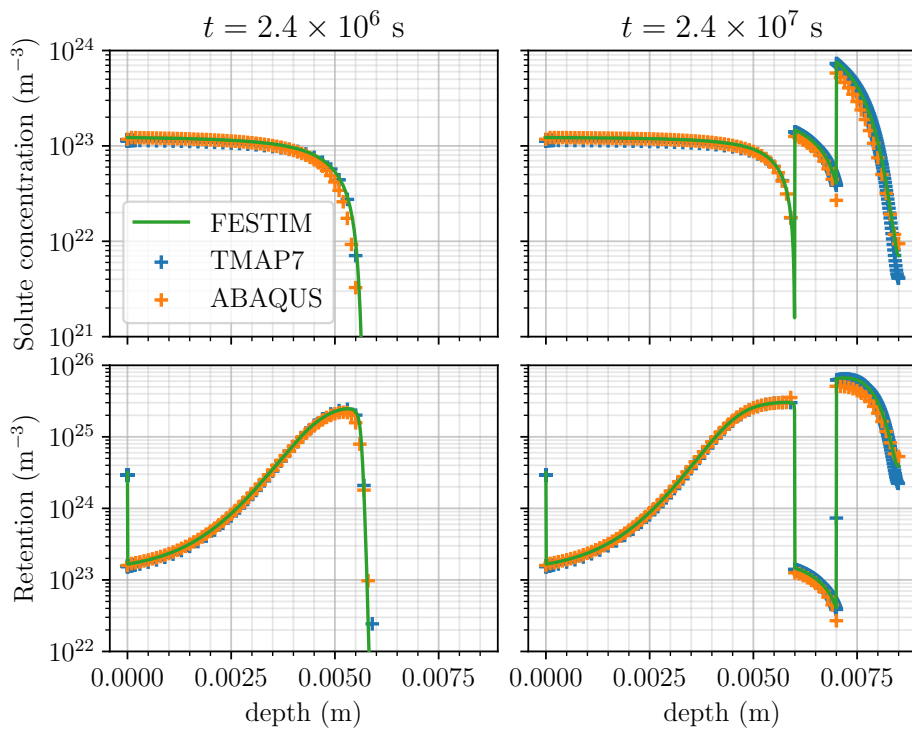
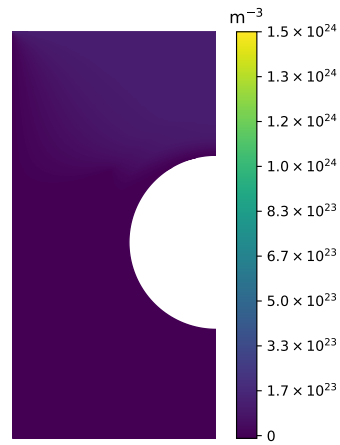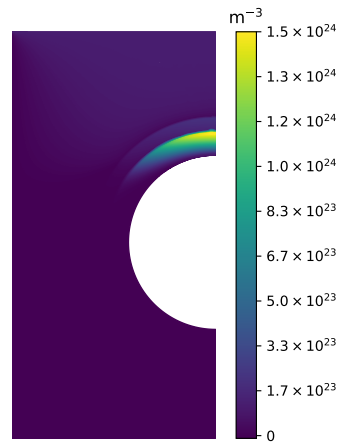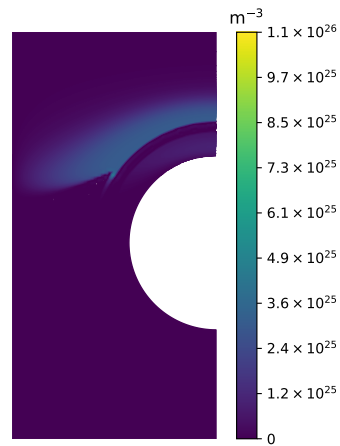Figure 8: Comparison of concentrations profiles at several times

12

Figure 9: Comparison of results provided by FESTIM, TMAP7 and ABAQUS
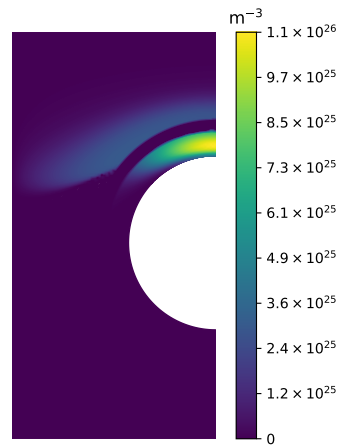
(a) c_{m} (continuity of c_{m})

(b) c_{m} (continuity of μ)

(c) Retention (continuity of c_{m})

(d) Retention (continuity of μ)

Figure 10: 2D concentration fields at $t = 2.4 \times 10^7\,\mathrm{s}$

6. Conclusion

The influence of interface conditions between materials has been studied with the code FESTIM. A novel approach has been implemented in FESTIM in order to ensure equilibrium at the interfaces. The implementation has been verified using the Method of Exact Solutions and the Method of Manufactured Solutions. A comparison test has been performed with TMAP7 and Abaqus and the three codes show very good agreement.

H transport through Cu/EUROFER and W/Cu composite slabs has been studied. It is shown that the interface condition can have an impact on the outgassing flux. This modelling work will help design future permeation barriers in DEMO. A method for identifying material properties with either an analytical solution or with the FESTIM code is also described.

The influence of interface conditions is also studied on the ITER monoblock test case in both 1D and 2D. It is shown that this has very low influence up to 5×10^6 s and that discrepancies only start to appear after a very long exposure time. This is because interfaces are far from the exposed surface and hydrogen atoms only reach these interface after a long exposure time. The continuity of mobile concentration can therefore be employed safely for monoblocks H transport simulations.

Future work will include modelling of ITER monoblocks in 3D with a focus on H outgassing from the gaps between monoblocks. A more thorough study regarding the permeation flux to the coolant will also be performed with a focus on the choice of a boundary condition at the cooling surface.

Authors' contribution

Rémi Delaporte-Mathurin: Methodology, Simulations, Analysis, Numerical Development, Writing. **Etienne Hodille**: Methodology, Analysis, Numerical Development, Writing, Review. **Jonathan Mougenot**: Bibliography, Writing, Methodology, Simulations, Review, project management. **Yann Charles**: Analysis, Numerical Development, Writing, Simulations, Review, Project management. **Gregory De Temmerman**: Definition of standard case, Code-code benchmark, Mentoring. **Floriane Leblond**: Experimental work, W/EUROFER Simulations. **Christian Grisolia**: Analysis, Review, Project management.

References

[1] Didier Perrault. Safety issues to be taken into account in designing future nuclear fusion facilities. *Fusion Engineering and Design*, 109-111:1733–1738, November 2016.

[2] C. Grisolia. Plasma wall interaction during long pulse operation in Tore Supra. *Journal of Nuclear Materials*, 266-269:146–152, March 1999.

[3] Sandeep Kumar Dwivedi and Manish Vishwakarma. Hydrogen embrittlement in different materials: A review. *International Journal of Hydrogen Energy*, 43(46):21603–21616, November 2018.

[4] G. De Temmerman, T. Hirai, and R. A. Pitts. The influence of plasma-surface interaction on the performance of tungsten at the ITER divertor vertical targets. *Plasma Physics and Controlled Fusion*, 60(4):044018, March 2018. Publisher: IOP Publishing.

[5] Sofiane Benannoune, Yann Charles, Jonathan Mougenot, Monique Gaspérini, and Greg De Temmerman. Multidimensional finite-element simulations of the diffusion and trapping of hydrogen in plasma-facing components including thermal expansion. *Physica Scripta*, T171:014011, January 2020.

[6] Sofiane Benannoune, Yann Charles, Jonathan Mougenot, and Monique Gaspérini. Numerical simulation of the transient hydrogen trapping process using an analytical approximation of the McNabb and Foster equation. *International Journal of Hydrogen Energy*, 43(18):9083–9093, May 2018.

[7] Rémi Delaporte-Mathurin, Etienne A. Hodille, Jonathan Mougenot, Yann Charles, and Christian Grisolia. Finite element analysis of hydrogen retention in ITER plasma facing components using FESTIM. *Nuclear Materials and Energy*, 21:100709, December 2019.

[8] Jonathan Shimwell, Rémi Delaporte-Mathurin, Jean-Charles Jaboulay, Julien Aubert, Chris Richardson, Chris Bowman, Andrew Davis, Andrew Lahiff, James Bernardi, Sikander Yasin, and Xiaoying Tang. Multiphysics analysis with CAD-based parametric breeding blanket creation for rapid design iteration. *Nuclear Fusion*, 59(4):046019, March 2019.

[9] C. San Marchi, B. P. Somerday, and S. L. Robinson. Permeability, solubility and diffusivity of hydrogen isotopes in stainless steels at high gas pressures. *International Journal of Hydrogen Energy*, 32(1):100–116, January 2007.

[10] Alfons H. M. Krom and Ad Bakker. Hydrogen trapping models in steel. *Metallurgical and Materials Transactions B*, 31(6):1475–1482, December 2000.

[11] Rion A Causey. Hydrogen isotope retention and recycling in fusion reactor plasma-facing components. *Journal of Nuclear Materials*, 300(2):91–117, February 2002.

[12] Song Jiangfeng, Huang Zhiyong, Li Lianxia, Chen Chang'an, and Luo Deli. One-dimensional simulation of hydrogen isotopes diffusion in composite materials by FVM. *International Journal of Hydrogen Energy*, 36(9):5702–5706, May 2011.

[13] Elsiddig Elmukashfi, Edmund Tarleton, and Alan C. F. Cocks. A modelling framework for coupled hydrogen diffusion and mechanical behaviour of engineering components. *Computational Mechanics*, 66(1):189–220, July 2020.

[14] Rémi Delaporte-Mathurin, E. A. Hodille, Jonathan Mougenot, Gregory De Temmerman, Yann Charles, and Christian Grisolia. Parametric study of hydrogenic inventory in the ITER divertor based on machine learning. *Scientific Reports*, October 2020.

[15] Dapeng Liu, Jing Wang, Ruiyang Liu, and S. B. Park. An examination on the direct concentration approach to simulating

15

moisture diffusion in a multi-material system. *Microelectronics Reliability*, 60:109–115, May 2016.

[16] Michael Smith. ABAQUS/Standard User's Manual, Version 6.9. 2009.

[17] Glen R. Longhurst. TMAP7 User Manual. Technical Report INEEL/EXT-04-02352, Idaho National Laboratory (INL), December 2008.

[18] R. Kirchheim and A. Pundt. 25 - Hydrogen in Metals. In David E. Laughlin and Kazuhiro Hono, editors, *Physical Metallurgy (Fifth Edition)*, pages 2597–2705. Elsevier, Oxford, January 2014.

[19] Martin Alnæs, Jan Blechta, Johan Hake, August Johansson, Benjamin Kehlet, Anders Logg, Chris Richardson, Johannes Ring, Marie E. Rognes, and Garth N. Wells. The FEniCS Project Version 1.5. *Archive of Numerical Software*, 3(100), December 2015.

[20] John D. Hunter. Matplotlib: A 2D Graphics Environment. *Computing in Science Engineering*, 9(3):90–95, May 2007. Conference Name: Computing in Science Engineering.

[21] Rémi Delaporte-Mathurin, Etienne A. Hodille, Jonathan Mougenot, Yann Charles, and Christian Grisolia. Parametric optimisation based on TPD experiments for rapid and efficient identification of hydrogen transport materials properties.

[22] R. Frauenfelder. Solution and Diffusion of Hydrogen in Tungsten. *Journal of Vacuum Science and Technology*, 6(3):388–397, May 1969.

[23] F. Reiter, K. S. Forcey, and G. Gervasini. *A compilation of tritium : Material interaction parameters in fusion reactor materials*. July 1996. Publisher: Publications Office of the European Union.

[24] E Serra and A Perujo. Hydrogen and deuterium transport and inventory parameters in a Cu–0.65Cr–0.08Zr alloy for fusion reactor applications. *Journal of Nuclear Materials*, 258-263:1028–1032, October 1998.

[25] A. Aiello, I. Ricapito, G. Benamati, and R. Valentini. Hydrogen Isotopes Permeability in Eurofer 97 Martensitic Steel. *Fusion Science and Technology*, 41(3P2):872–876, May 2002.

[26] E. A. Hodille, X. Bonnin, R. Bisson, T. Angot, C. S. Becquart, J. M. Layet, and C. Grisolia. Macroscopic rate equation modeling of trapping/detrapping of hydrogen isotopes in tungsten materials. *Journal of Nuclear Materials*, 467:424–431, December 2015.

[27] T.J. Dolan and R.A. Anderl. Assessment of database for interaction of tritium with ITER plasma facing materials. Technical Report EGG-FSP–11348, 10191406, September 1994.

[28] R. A. Anderl, M. R. Hankins, G. R. Longhurst, and R. J. Pawelko. Deuterium transport in Cu, CuCrZr, and Cu/Be. *Journal of Nuclear Materials*, 266-269:761–765, March 1999.

[29] Pauli Virtanen, Ralf Gommers, Travis E. Oliphant, Matt Haberland, Tyler Reddy, David Cournapeau, Evgeni Burovski, Pearu Peterson, Warren Weckesser, Jonathan Bright, Stéfan J. van der Walt, Matthew Brett, Joshua Wilson, K. Jarrod Millman, Nikolay Mayorov, Andrew R. J. Nelson, Eric Jones, Robert Kern, Eric Larson, C. J. Carey, Ìlhan Polat, Yu Feng, Eric W. Moore, Jake VanderPlas, Denis Laxalde, Josef Perktold, Robert Cimrman, Ian Henriksen, E. A. Quintero, Charles R. Harris, Anne M. Archibald, Antônio H. Ribeiro, Fabian Pedregosa, and Paul van Mulbregt. SciPy 1.0: fundamental algorithms for scientific computing in Python. *Nature Methods*, 17(3):261–272, March 2020. Number: 3 Publisher: Nature Publishing Group.

[30] Alan C. Hindmarch. ODEPACK, A Systematized Collection of ODE Solvers. *Scientific Computing*, pages 55–64, 1982.

[31] Elisabeth Vasikaran, Yann Charles, and Pierre Gilormini. Implementation of a reaction-diffusion process in the Abaqus finite element software. *Mechanics & Industry*, 21(5):508, 2020. Number: 5 Publisher: EDP Sciences.

[32] Chang-Sik Oh, Yun-Jae Kim, and Kee-Bong Yoon. Coupled Analysis of Hydrogen Transport using ABAQUS. *Journal of Solid Mechanics and Materials Engineering*, 4(7):908–917, 2010.

Appendix A. Transient model

Appendix A.1. Model description

A kinetic model of trapping/detrapping at the interface between two materials based on the idealised energy diagram shown in Figure A.11 is presented. On this diagram, $E_{\mathrm{diff},k}$ is the barrier for the diffusion of H from interstitial site to interstitial site, $E_{k\to i}$ is the trapping energy from material k to the interface, $E_{i\to k}$ is the detrapping energy from the interface to the interface and $E_{S,k}$ is the solution energy of H in material k. In this model, H is split into three populations: the concentrations of mobile H in materials 1 & 2 (c_1 and c_2 respectively) expressed in m^{-3} and the concentration of H trapped at the interface c_i (in m^{-2}). The interface coverage is defined as: $\theta_i = \frac{c_i}{n_i}$ where
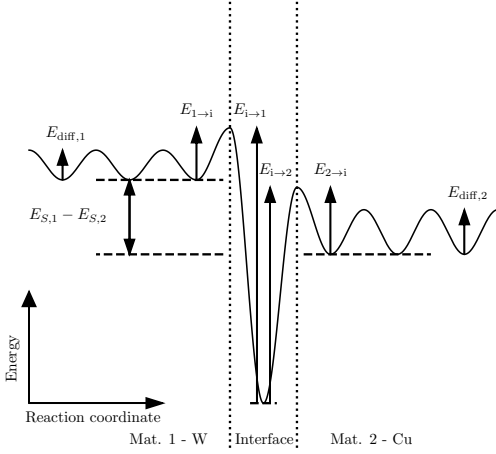

Figure A.11: Idealised potential energy diagram describing the interactions of H at the interface between two materials. In this case, $E_{\mathrm{S},1} > E_{\mathrm{S},2}$ (consistent with a W/Cu interface Table 1).

n_i is the sites concentration on the interface (in m^{-2}). The interface is considered as a 2D defect (like a surface), hence the unit of c_i and n_i is m^{-2}.

In this model, 2 types of reactions are considered at the interface:

- the trapping from material k to the interface: $H_k \to H_i$.

- the detrapping from the interface to material k: $H_i \to H_k$.

The rate (s^{-1}) of each reaction $x \to y$ is written with an Arrhenius law:

$$\nu_{x\to y}(T) = \nu_0^{x\to y} \exp\left(-\frac{E_{x\to y}}{k_B T}\right) \qquad (A.1)$$

with $\nu_0^{x\to y}$ (s^{-1}) the pre-exponential factor, $E_{x\to y}$ (eV) the energy barrier for the reaction $x \to y$, k_B ($\mathrm{eV\,K^{-1}}$)

the Boltzmann constant and T (K) the temperature.

The jump from interstitial site to interstitial site in material k is assumed to be described by the Fick's law on diffusion characterised by the diffusion coefficient of H in material k $D_{k\in\{1,2\}}$ ($\mathrm{m^2\,s^{-1}}$). Thus, the flux balance at the interface gives:

$$\lambda_1\left(\frac{\partial c_1}{\partial t}\right)_{x_i} = \nu_{i\to 1}c_i - \lambda_1 c_1(1-\theta_i)\nu_{1\to i}$$
$$- D_1\left(\frac{\partial c_1}{\partial x}\right)_{x_i} \qquad (A.2)$$

$$\frac{dc_i}{dt} = \lambda_1 c_1(1-\theta_i)\nu_{1\to i} - \nu_{i\to 1}c_i$$
$$+ \lambda_2 c_2(1-\theta_i)\nu_{2\to i} - \nu_{i\to 2}c_i \qquad (A.3)$$

$$\lambda_2\left(\frac{\partial c_2}{\partial t}\right)_{x_i} = \nu_{i\to 2}c_i - \lambda_2 c_2(1-\theta_i)\nu_{2\to i}$$
$$+ D_2\left(\frac{\partial c_2}{\partial x}\right)_{x_i} \qquad (A.4)$$

where $\lambda_{k\in\{1,2\}}$ (m) is the distance between two interstitial sites in material k (such that $\lambda_k c_k(x_i)$ represent the areal density of interstitial H at the depth x_i which interacts with the interface). In Equations A.2 and A.4, the first term on the right-hand side corresponds to the detrapping from the interface to material k, the second term correspond to the trapping to the interface and the last term corresponds to the diffusion that carries away particles from the interface region (it is important to note that the signs of these fluxes are different).

At steady-state, when the time derivatives are null and the diffusive flux can be neglected (i.e. when the diffusion depth is long compared to λ_k), one gets:

$$\frac{c_2}{c_1} = \frac{\lambda_1}{\lambda_2}\frac{\nu_{i\to 2}(T)}{\nu_{2\to i}(T)}\frac{\nu_{1\to i}(T)}{\nu_{i\to 1}(T)} = \frac{S_2(T)}{S_1(T)} \qquad (A.5)$$

with $S_k(T)$ ($\mathrm{m^{-3}\,Pa^{-0.5}}$) the solubility of H in material k. The condition to have such steady-state is:

$$E_{S,1} - E_{S,2} = E_{i\to 1} - E_{i\to 2} - E_{1\to i} + E_{2\to i} \qquad (A.6)$$

Appendix A.2. Test case

The simple kinetic presented here allows us to see how fast the equilibrium given by Equation 5 is reached. For the test case, we further simplify the model by considering that the concentration of interstitial H in material 1 c_1 is constant (*ie.* $\partial c_1/\partial t = 0$). The diffusive fluxes are neglected in Equation A.4 in order to solve a 0D problem. The system of equation is solved with the SciPy package [29] which uses the odepack library [30].

A W/Cu interface is simulated at $475\,\mathrm{K}$. All parameters in the model have been constrained so that it corresponds to the steady state condition in equation A.6 in the case of a W/Cu interface considering for both W and Cu,

$E_{k\to i} = E_{\mathrm{diff},k}$ with k=Cu or W. The values of λ for W and Cu are 110 pm and 65 pm respectively. The concentration of H in W is set to $c_1 = 10^{18}\,\mathrm{m}^{-3}$. The concentration of trapping site at the interface is set to $n_i = 10^{19}\,\mathrm{m}^{-2}$. All pre-exponential factors are set to $10^{13}\,\mathrm{s}^{-1}$. The only free parameter left is $E_{i\to,2}$ and a parametric study is performed (see Figure A.12).

The ratio c_2/c_1 steady state value is approximately 10^5 (see Figure A.12(a)). The ratio $\theta_i/\theta_i^{\mathrm{eq}}$ does not depend on the value of the detrapping energy (see Figure A.12(b)). τ_i and τ_2 are defined as the time at which c_i and c_2 have reached 95% of their equilibrium value. In this case, both τ_i and τ_2 remain below $10^3\,\mathrm{s}$ (see Figure A.12(c)). The interface is saturated with H for $E_{i\to,2}/(k_B T) > 25$ (see Figure A.12(d)).

Appendix B. Implementation of the C/S continuity in Abaqus Finite Element Software

The Abaqus implementation scheme to be able to solve simultaneously a transient heat transfers problem along a transient hydrogen transport and trapping one is described in [5]. It is based on the introduction of muti-diffusion capabilities [31] through user Subroutines developments [16]. The global implementation scheme is not described in this appendix, which is limited to the implementation of the transient transport and trapping process in the UMATHT subroutine, ensuring the continuity of c_m/S where S is the solubility and c_m the solute hydrogen concentration.

Appendix B.1. Equations

The total hydrogen concentration is

$$c = c_m + \sum_i c_{t,i} \tag{B.1}$$

To force the c_m/S continuity in the Abaqus software, the degree of freedom for diffusion numbered 11 is set to c_m/S instead of c_m. The transport and trapping equation, which is

$$\frac{\partial c}{\partial t} = \nabla \cdot (D\nabla c_m) \tag{B.2}$$

is thus rewritten as

$$S\frac{\partial \phi}{\partial t} + \phi\frac{dS}{dT}\frac{\partial T}{\partial t} + \sum_i \frac{\partial c_{t,i}}{\partial t} = \nabla \cdot \left(DS\nabla\phi + D\phi\frac{dS}{dT}\nabla T \right) \tag{B.3}$$

where $\phi = c_m/S$. Hydrogen flux is thus

$$\varphi = -DS\nabla\phi - D\phi\frac{dS}{dT}\nabla T \tag{B.4}$$

Appendix B.2. UMATHT implementation

The reader should refers to [32] for a global presentation of the UMATHT development, internal variables, and underling analogy.
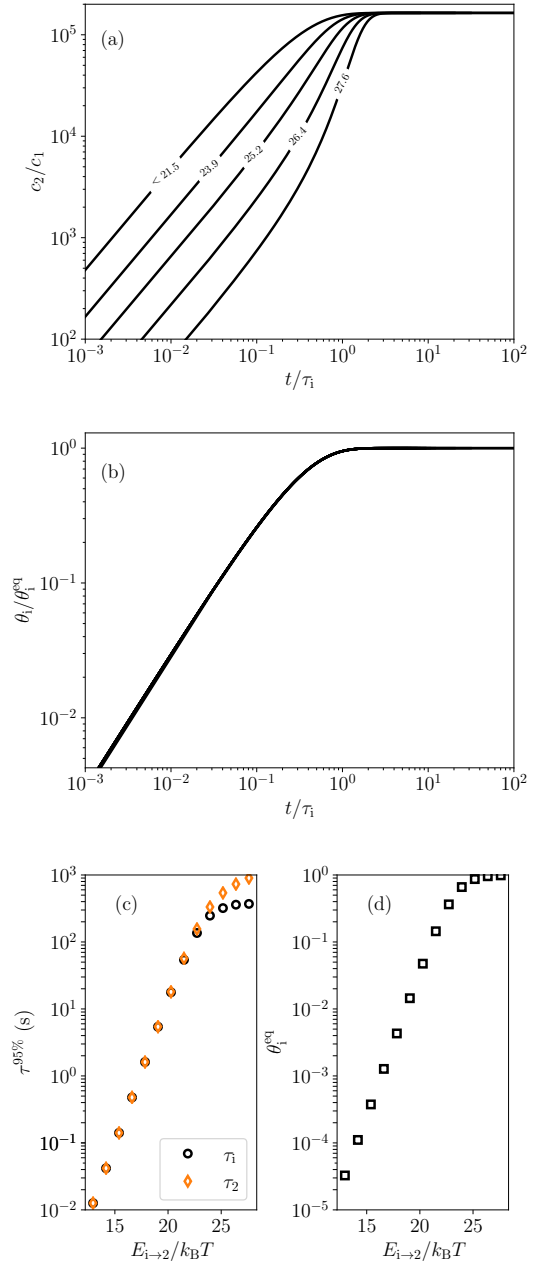

Figure A.12: (a) Evolution of the ratio c_2/c_1 with normalised time t/τ_i for different values of $E_{i\to2}/k_B T$. (b) Evolution of the ratio $\theta_i/\theta_i^{\mathrm{eq}}$ with normalised time t/τ_i (independent of $E_{i\to2}/k_B T$). (c) Evolution of the time to reach 95% of the steady-state concentration, τ_i and τ_2 as a function of $E_{i\to2}/k_B T$. (d) Evolution of θ_i^{eq} as a function of $E_{i\to2}/k_B T$. The temperature in the simulation is 475 K, the concentration in the material 1 (W) is $c_1 = 10^{18}\,\mathrm{m}^{-3}$ and the concentration of trapping site at the interface is $n_i = 10^{19}\,\mathrm{m}^{-2}$.

The *temp* variable is set to $\phi = c_m/S$, and *dtemp* to $d\phi = d(c_m/S) = dc_m/S - c_m dS/S^2$.

The hydrogen flux has been defined in the previous

section, and thus $dfdt$ and $dfdg$ variables are so that

$$dfdt = \frac{\partial \varphi}{\partial \phi} = -D\frac{dS}{dT}\nabla \mathbf{T} \qquad (\text{B.5})$$

and

$$dfdg = \frac{\partial \varphi}{\partial \nabla \phi} = -(DS)\,\mathbf{I} \qquad (\text{B.6})$$

u is so that $u = c$, leading to the following incremental relationship

$$u(t + \delta t) = u(t) + (dudt)\delta \phi + \phi \frac{dS}{dT}\delta T \qquad (\text{B.7})$$

where $dudt$ is so that

$$dudt = \frac{\partial c}{\partial \phi} = S\left(1 + \sum_i \frac{\partial c_{\text{t},i}}{\partial c_{\text{m}}}\right) \qquad (\text{B.8})$$

Last, in the context of transient trapping, $\partial c_{\text{t},i}/\partial c_{\text{m}}$ is computed using the Generalized Oriani's Approximation (GOA), as defined in [6].